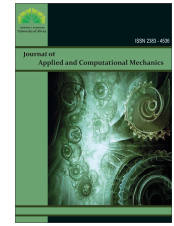




Journal of Applied and Computational Mechanics



Research Paper

Numerical and Artificial Neural Network Analysis of Magnetohydrodynamic Natural Convection in a Nano-encapsulated Phase Change Suspension Filled Quadrantal Circular Enclosure

Mehdi Ghalambaz¹, Ioan Pop², Mikhail Sheremet³, Mohammed Hasan Ali⁴,
Mohammad Ghalabaz³

¹ Department of Mathematics, Saveetha School of Engineering, SIMATS, Chennai, India, Email: ghalambaz.mehdi@gmail.com

² Department of Mathematics, Babes-Bolyai University, 400084 Cluj-Napoca, Romania, Email: ipop@math.ubbcluj.ro

³ Laboratory on Convective Heat and Mass Transfer, Tomsk State University, 634050 Tomsk, Russia, Email: sheremet@math.tsu.ru (M.S.); m.ghalambaz@gmail.com (M.G.)

⁴ College of Technical Engineering, Imam Ja'afar Al-Sadiq University, Al-Muthanna 66002, Iraq, Email: mh180250@gmail.com

Received October 16 2024; Revised November 30 2024; Accepted for publication December 03 2024.

Corresponding authors: I. Pop (ipop@math.ubbcluj.ro)

© 2024 Published by Shahid Chamran University of Ahvaz

Abstract. This article deals with the heat transfer dynamics of a quadrantal circular enclosure filled with nano-encapsulated phase change material (NEPCM) suspension. Central to the investigation is the examination of nanoparticles that exhibit phase transitions and their consequential effects on the thermophysical attributes of the NEPCM suspension. The transformative states of these nanoparticles - solid, liquid, or phase change - are pivotal in modifying localized heat capacity, influenced by various parameters. Among these, the concentration of NEPCM particles, the Rayleigh number, the Hartmann number, and the fusion temperature stand out as critical to heat transfer dynamics. The governing equations for fluid flow and heat transfer of NEPCM suspension are introduced in the form of partial differential equations and were solved using the finite element method. The results showed that while an increase in the Rayleigh number augments heat transfer rates, a rise in the Hartmann number reduces it due to the Lorenz force's influence on fluid velocity. Optimal fusion temperature values, crucial to heat transfer, have been pinpointed at $\theta_f = 0.35$ and $\theta_f = 0.675$. The study further unveils the augmentation in heat transfer rates with an increased concentration of nanoparticles, particularly at the wall's commencement. A significant contribution is developing a neural network model, demonstrating high predictive accuracy for heat transfer rates. This model, through contour diagrams, offers insights into heat transfer dynamics, sidestepping the need for extensive numerical simulations.

Keywords: Heat transfer enhancement; Magnetohydrodynamic; Nano encapsulated phase change suspensions; Free convection; Composite nanoparticles.

1. Introduction

The phase change can contribute to heat transfer through the latent heat of fusion. In some cases, the phase change material is used in enclosures to store thermal energy. In these cases, the mixture of some phase change materials [1] or using nanoparticles [1, 2] and other heat transfer enhancement approaches are required to improve the heat transfer [3]. Another approach is the nano encapsulation of phase change material so they can be suspended in a host fluid and improve the heat capacity and heat transfer properties of the host fluid [4, 5]. The growing need for energy-efficient and sustainable technologies has brought nano-encapsulated phase change material (NEPCM) suspensions to the forefront of heat transfer and energy storage research. As evidenced by the rich body of research on NEPCM, these innovative suspensions show promising advancements in heat storage and transfer applications.

1.1. NEPCM suspensions heat transfer and energy storage

A study by Sharma et al. [6] illustrates the potential of NEPCM suspensions in solar energy storage. They discovered that NEPCM reduces charging and discharging times by 21% and 23%, respectively. The instantaneous efficiencies improved by up to 24% and 28%, indicating its high potential for applications like off-time hot water supply and milk pasteurization. Alhashash and Saleh [7] further expand on the potential of NEPCM suspensions in enhancing conjugate heat transfer in heated enclosures. By utilizing NEPCM in a differentially heated enclosure with an active cylinder, they found that the optimal positioning of the cylinder and NEPCM concentration significantly impacted heat transfer.



NEPCM suspensions have also found applications in the electronics industry. Almutairi [8] demonstrated that embedding integrated circuits within an inclined cavity using NEPCM significantly improved the heat transfer process. They observed a total heat transfer rate increase of 29% with a 3% volume fraction of NEPCM at a Rayleigh number of 104. Adding just 5% NEPCM particles can enhance heat transfer by 25% in boundary layer flows, with the transition temperature playing a crucial role in this improvement [9].

NEPCM suspensions not only enhance heat transfer but also increase energy storage efficiency. Zhang et al. [10] highlighted the thermal performance of NEPCM suspensions, with the best-performing NEPCM4 having a melting enthalpy heat of 171.8 J/g and encapsulation efficiency of 76.1%. Such properties make NEPCMs ideal for heat transfer and energy storage applications.

Furthermore, integrating NEPCM with various materials can yield added advantages. Shajahan et al. [11] observed that the inclusion of silver nanoparticles in PCM led to a boost in drinking water production by 16% and enhanced the thermal efficiency of the double-slope solar still by 62.53%. A study by Jain and Parhizi [12] provided a theoretical examination of heat transfer during phase change in spherically encapsulated PCM, emphasizing the promising capabilities of NEPCM mixtures. The study underlines that the encapsulant thickness, thermal properties, and external boundary conditions are all factors that influence phase change propagation. In the context of the thermal management of electronic devices, Qaderi and Veysi [13] proposed a thermal management system for 18650 Li-ion batteries using NEPCM. The study highlighted that the operating conditions of the Battery Thermal Management System (BTMS), such as low Reynolds number and heat transfer coefficient, moderate discharge rate, and ambient temperature close to the PCM's solidus temperature, could be optimized using this technology. Cao et al. [14] found that adding NEPCM to water augmented the heat transfer rate by 10.43%, 19.1%, and 18.3% for Rayleigh numbers 102, 104, and 106, respectively, demonstrating the NEPCM's effectiveness in improving heat transfer in energy storage systems.

In a study by Golab et al. [15], the impact of introducing NEPCM to water during natural convection within a rectangular cavity was explored. Their findings indicated that the integration of NEPCM can amplify heat transfer by as much as 48%. The optimum heat transfer was observed when the energy wall was positioned at the cavity's midpoint. Additionally, they suggested a relationship for the thermal expansion coefficient of NEPCM, factoring in the thermal expansion coefficients of both the core and shell materials. In a related study, Aly et al. [16] probed into the influence of magnetic fields and thermal radiation on the double diffusion of a solid phase within a unique cavity configuration comprising two interconnected circular cylinders infused with both NEPCM and porous media. They concluded that both thermal radiation and magnetic fields play a significant role in altering the double diffusion mechanism. Changes in the fractional time-derivative parameter notably affected the heat and mass transfer, as well as the behavior of the nanofluid in the early stages. Furthermore, a surge in the Rayleigh number was found to elevate the nanofluid's temperature, concentration, and velocity within the cavity. Abderrahmane et al. [17] took a different approach, exploring 2D mixed convection in a zigzagged trapezoidal chamber using NEPCM. The study showed a parabolic behavior of the melt band curve at smaller Reynolds numbers and larger Hartmann numbers, with minimizing the wave number found to be beneficial in achieving a higher heat transfer rate.

1.2. NEPCMs and magnetic field effects

The utilization of NEPCM suspensions is not limited to thermal management and energy storage applications. Jiang et al. [18] described NEPCM suspensions with magnetic responsiveness, making them suitable for applications like rapid magnetic localization temperature regulation, magnetic separation recycling, and solar energy conversion. The field of NEPCM has seen significant discoveries made towards enhancing heat transfer efficiency and storage capacity. Notable researches in this domain have shown promising potential for applying NEPCM in various sectors.

Considering the MHD (Magnetohydrodynamic) natural convection heat transfer of NEPCM suspensions, Shin et al. [19] pioneered a novel thermal energy transport system, which showed a remarkable increase in thermal energy conveyance per unit flow rate, reaching up to 180%. This attested to the system's efficacy and dependability. Meanwhile, Wang et al. [20] researched an efficient photothermal conversion capric acid PCM microcapsule, promising significant advancements in energy storage systems. Abderrahmane et al. [17] studied 2D MHD mixed convection in a zigzagged trapezoidal chamber. They found that the melt band curve parabolically behaves at a smaller Reynolds number (Re) and larger Hartmann number (Ha), providing insight into optimizing heat transfer rates.

Aly et al. [21] explored the effects of an inclined magnetic field on double-diffusive convection of NEPCM in an annulus between two super ellipses. They concluded that an increase in the magnetic field and aspect ratio can significantly affect heat/mass transmission and nanofluid movements. Similarly, Raizah and Aly [22] studied the influence of dual-rotation on NEPCM's MHD free convection in a hexagonal-shaped enclosure, finding that certain parameters like fin length, fusion temperature $\theta(f)$, and Hartmann number Ha, can positively impact the mean Nusselt number (Nu). Lastly, Alazzam et al. [23] highlighted that the heat transfer within a rectangular wavy enclosure was most affected by the Rayleigh number (Ra) and Hartmann number (Ha), which is crucial for designing and optimizing energy storage systems using NEPCM suspension.

1.3. Heat transfer of NEPCMs in enclosures

The scientific investigation of NEPCM suspensions reveals the impact of various geometries and boundary conditions on the overall phase change process. For example, the natural convection of NEPCM was further explored by Aly and Alsedais [24] in a partial porous H-shaped cavity using ISPH simulation. The heat capacity contours within the cavity were found to be controlled by hot source length, Rayleigh number, and fusion temperature. On the other hand, Shehzad et al. [25] utilized wing-like fins in a heat exchanger and discovered that vertical alignment enhanced thermal performance.

Ahmed and Khamis [26] examined the entropy generation and convective flow in an inclined prismatic container filled with NEPCM. The research revealed that a particular design could lead up to a 36% reduction in the stream functions' maximum values. Aly et al. [27, 28] studied more complex geometries like a porous infinite-shaped enclosure and a tall fin inside two circular [28] cylinders, respectively. Both studies pointed towards the influence of multiple parameters, including fusion temperature and the Darcy parameter, on the phase change zone and heat distribution. The works of Raizah and Aly [29] similarly underlined the effects of changing geometries, like an annulus between two circular cylinders and a rotating super ellipse inside a hexagonal-shaped cavity, on heat and concentration transfer. Aly et al. [21] also employed unique geometry, using an annulus between two super ellipses, and identified various influential factors, such as the magnetic field and Rayleigh number, on the double-diffusive convection of NEPCM.

The literature review highlights a notable lack of research on the subject of entropy generation in NEPCM suspensions when exposed to a magnetic field. Venturing into uncharted territory, this research aims to bridge this gap in understanding by exploring how entropy generation occurs in NEPCMs when subjected to a non-uniform magnetic field within a quadrantal enclosure.



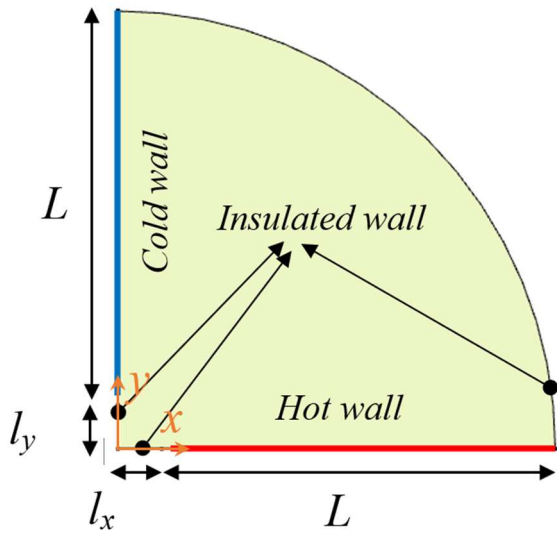


Fig. 1. A diagram of enclosure, physical domain and boundary conditions.

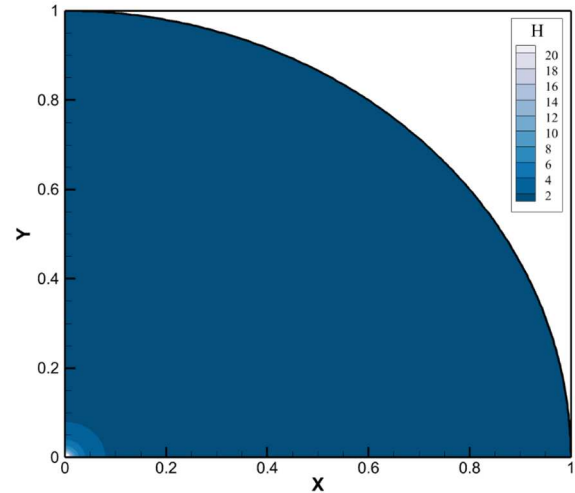


Fig. 2. A view of the non-uniform magnetic field (H) due to the presence of a magnetic source at the corner $(0,0)$.

2. Physical Model

A quadrantal circular enclosure is uniformly filled with a NEPCM suspension of concentration ϕ . The left vertical wall maintains a consistently cold temperature T_c , whereas the bottom horizontal wall is at a uniformly hot temperature T_h . The other wall is thoroughly insulated as depicted in Fig. 1. The present geometry was adopted following the study of Dutta et al. [31] for MHD flow of Cu-water nanofluid.

Buoyancy forces initiate a natural convection current that originates from the heated lower wall and ascends to reach the cooler left wall. The cooled suspension at this cold wall then descends towards the heated base, thereby completing the cycle. The warm wall mimics the role of electronic components, while the cold walls are responsible for regulating the system's temperature. This regulation occurs either via releasing heat into the environment or by employing radiators.

The nanoparticles are designed with a core composed of PCM, which permits them to experience a phase transition while suspended in the carrier fluid. As a result, these nanoparticles exert a transformative effect on the nanofluid's (NEPCM-suspension) thermophysical attributes, including dynamic viscosity and thermal conductivity, while also influencing the localized heat capacity. The said heat capacity varies with temperature and is directly impacted by the phase change temperature, represented as T_m , of the PCM-based nanoparticle cores. These temperature-sensitive properties of the nanoparticles enhance distinctive cooling efficiencies and energy storage potential.

Figure 1 presents a depiction of the phase change process occurring within the core of a nanoparticle immersed in a host fluid. The nanoparticle's core can transition through multiple states - solid, liquid, or in the midst of a phase change - as it navigates through the host medium. The model specifically looks at a setup where the channel's sidewalls are maintained at a lower temperature, T_c (where T_c is less than T_m), while the inner duct's sidewall is kept at a higher temperature, T_h (where T_h is greater than T_m). There is also a magnetic source term positioned at the origin, which is the corner of the enclosure, as indicated in Fig. 1.

To define the magnetic field's intensity, it's postulated that the magnetic source aligns with a vertically standing magnetic wire situated at the heart of the coordinate system. The overall magnetic field strength (H) and the components of magnetic field intensity (H_y and H_x) can be delineated as follows [27, 28]:

$$H'_x = \frac{\gamma}{2\pi} \left(\frac{1}{x^2 + y^2} \right) y, H'_y = -\frac{\gamma}{2\pi} \left(\frac{1}{x^2 + y^2} \right) x \quad (1)$$

where $H' = \sqrt{H'^2_x + H'^2_y}$ and γ indicates the magnetic strength. Figure 2 presents a visual representation of a non-uniform magnetic field (H) due to a magnetic source at the corner $(0,0)$. As the illustration shows, the magnetic field exhibits a high intensity at the corner near the source. However, as the distance from the corner increases, there is a steep decline in its strength. This change in magnetic field intensity follows a semi-circular distribution that emanates from the source. Essentially, the magnetic field's influence radiates outwards from the corner, creating a kind of ripple effect where the strongest magnetic pull is at the source, and it progressively weakens as you move further away.

Owing to their diminutive size, the encapsulated particles exhibit virtually negligible internal temperature gradients. This property makes them uniquely suitable for use in lamp models where nanoparticle-mediated phase changes are implemented. A list of characteristics of the host fluid and nanoparticles is provided in Table 1. The NEPCM cores phase change temperature and latent heat of phase change are 32°C and 211 kJ/kg , respectively [32].

In the present setup, the functioning fluid is deemed Newtonian, demonstrating laminar flow behavior, and both the host fluid and the particles are treated as incompressible substances [33, 34]. To account for the system's buoyancy forces, the Boussinesq approximation is employed. Bearing these considerations in mind, the following section furnishes the mathematical formulation for representing the natural convection heat transfer of the NEPCM-suspension within the cavity. These equations provide the theoretical framework for analyzing the heat transfer processes at play in this configuration.

Table 1. List of material properties (Athanasopoulos et al. [30], Barlak et al. [32], Sheikholeslami et al. [35]).

	ρ (kg/m ³)	C_p (KJ/kg.K)	σ ($\Omega.m$) ⁻¹	μ (kg/m. s)	β (K ⁻¹)	k (W/m.K)
Particle Shell (PU)	786	1317.7	10^{-6}	---	17.28×10^{-5}	---
Host (Water)	997.1	4179	0.05	8.9×10^{-4}	21×10^{-5}	0.613
Particle core (Nonadecane)	721	2037	---	---	---	---



2.1. Model equations

The dynamics of fluid flow in this investigation are captured through the integration of continuity and momentum equations, adopting the methodology proposed in Ghalambaz et al. [33]. Moreover, the effects of buoyancy forces are factored in by accounting for a body force that varies with temperature. The implications of magnetic fields are also incorporated into the momentum equation via body force source terms, as detailed in [27, 33-35].

Continuity equation:

$$\nabla \mathbf{u} = 0 \quad (2)$$

Momentum equation:

$$\rho_{npcm} (\mathbf{u} \cdot \nabla) \mathbf{u} = -\nabla p + \mu_{npcm} \nabla^2 \mathbf{u} + \mathbf{f}_B + \mathbf{f}_M \quad (3)$$

Heat equation:

$$(\rho C_p)_{npcm} \mathbf{u} \cdot \nabla T = k_{npcm} \nabla^2 T + q_M \quad (4)$$

where the buoyancy force (\mathbf{f}_B) and MHD forces (\mathbf{f}_M) are introduced as:

$$\mathbf{f}_B = \begin{cases} x : 0 \\ y : \rho_{npcm} \beta_{npcm} g (T - T_c) \end{cases} \quad \text{and} \quad \mathbf{f}_M = \begin{cases} x : -\sigma_b B_y^2 u + \sigma_b B_x B_y v \\ y : +\sigma_b B_x B_y u - \sigma_b B_x^2 v \end{cases} \quad (5)$$

in which B is the magnetic induction with the components of $B_x = \mu_0 H_x^*$ and $B_y = \mu_0 H_y^*$ [35]. The velocity vector (\mathbf{u}) and field variables of pressure (p) and temperature (T) were used in the above equations. The gravity acceleration (g) was used in the buoyancy term. The thermophysical properties are the electrical conductivity (σ), volume expansion (β), thermal conductivity (k), specific heat (C_p), dynamic viscosity (μ), and density (ρ). The subscript $npcm$ denotes the NEPCM-suspension. The heat source due to the magnetic effects was introduced in the energy equations as defined in [27, 33-35]:

$$Q_M = \sigma_{npcm} (u B_y - v B_x)^2 \quad (6)$$

where u and v are the horizontal and vertical velocity components, respectively.

The equation presented below demonstrates the process for entropy production, encompassing both local thermal entropy generation and local friction entropy generation [36], denoted as:

$$s_l = s_u + s_T = \frac{\mu_{npcm}}{T_0} \left[2 \left(\left(\frac{\partial u}{\partial x} \right)^2 + \left(\frac{\partial v}{\partial y} \right)^2 \right) + \left(\frac{\partial u}{\partial y} + \frac{\partial v}{\partial x} \right)^2 \right] + \frac{k_{npcm}}{T_0^2} \left[\left(\frac{\partial T}{\partial x} \right)^2 + \left(\frac{\partial T}{\partial y} \right)^2 \right] \quad (7)$$

In this equation, s_T and s_u represent entropy generations stemming from the temperature gradient and the friction between fluid layers, respectively.

Ultimately, the employed boundary conditions are zero velocity ($u = 0$) at all surfaces and a reference pressure of $p = 0$ at the enclosure corner. The zero-heat flux at the curved surface $\partial T / \partial n$ and isotherms at the heated surface ($T = Th$) and cold surface ($T = Tc$) were applied.

2.2. Closure relationships for the suspension

The suspension is regarded as a homogenous blend of NEPCM particles and the carrier liquid, water [33]. The effective thermophysical properties were determined and used based on the data delineated in Table 2. The subscript of host indicates the host fluid (water), and the subscripts of core, shell, and particle represent the NEPCM core, NEPCM shell, and the NEPCM particle, respectively.

Table 2. The adopted relationships for the suspension thermophysical properties.

Property	Reference	Formula	Num.
suspension's specific heat capacity	[37, 38]	$Cp_{npcm} = \rho_{npcm}^{-1} (\rho_{host} Cp_{host} (1 - \varphi) + \rho_{particle} Cp_{particle} \varphi)$	(8)
NEPCM particles' density	[39]	$\rho_{particle} = (1 + \iota) (\rho_{core} \rho_{shell}) / (\rho_{shell} + \iota \rho_{core})$	(9)
suspension's density	[39]	$\rho_{npcm} = (1 - \varphi) \rho_{host} + \varphi \rho_{particle}$	(10)
suspension thermal expansion	[40]	$\beta_{npcm} = (1 - \varphi) \beta_{host} + \varphi \beta_{particle}$	(11)
specific heat capacity of NEPCM particles core	[39, 40]	$Cp_{particle} = Cp_{core} + \left\{ \frac{\pi}{2} \cdot \left(\frac{h_{sf}}{T_{\delta T}} - Cp_{core} \right) \sin \left(\pi \frac{T - T_f + \delta T/2}{\delta T} \right) \right\} \zeta$ $\zeta = \begin{cases} 0 & T < Tm - \delta T/2 \\ 1 & Tm - \delta T/2 < T < Tm + \delta T/2 \\ 0 & T > Tm + \delta T/2 \end{cases}$	(12)
suspension dynamic viscosity	[33, 41, 42]	$\frac{\mu_{npcm}}{\mu_{host}} = Nu \varphi + 1$	(13)
suspension thermal conductivity	[33, 41, 42]	$\frac{k_{npcm}}{k_{host}} = Nc \varphi + 1$	(14)
suspension electrical conductivity	[35]	$\frac{\sigma_{npcm}}{\sigma_{host}} = 1 + \left[3 \left(\frac{\sigma_{particle}}{\sigma_{host}} - 1 \right) f \right] / \left[\left(\frac{\sigma_{particle}}{\sigma_{host}} + 2 \right) - \left(\frac{\sigma_{particle}}{\sigma_{host}} - 1 \right) f \right]$	(15)



The weight ratio between the core and shell, represented by ι , is roughly valued at 0.447 [32]. Here, δT symbolizing the phase transition temperature interval, is instituted to maintain continuity in energy equilibrium, with its value selected as $\delta T / (Th - Tc) = 0.05$ [33]. In addition, hsf signifies the latent heat associated with the NEPCM particle cores.

2.3. Dimensionless form of equations

To offer a generalized portrayal of the behavior exhibited by the NEPCM suspension, the governing equations along with their respective boundary conditions can be converted into a dimensionless form. This requires the introduction of certain non-dimensional parameters which aid in achieving this transformation:

$$(X, Y, L_x, L_y) = \frac{(x, y, L_x, L_y)}{L}, U = \frac{uL}{\alpha_f}, V = \frac{vL}{\alpha_f}, P = \frac{pL^2}{\rho_f \alpha_f^2}, \theta = \frac{T - T_c}{Th - T_c}, H = \frac{H^*}{H_0}, H_x = \frac{H_x^*}{H_0}, H_y = \frac{H_y^*}{H_0}, \theta_m = \frac{Tm - Tc}{(Th - Tc)} \quad (16)$$

in which $H_0 = H^*(0, 0) = \gamma / 2\pi L$. Upon substituting the dimensionless variables into the governing equations, a sequence of non-dimensional governing equations was subsequently formulated:

$$\nabla U = 0 \quad (17)$$

Momentum equation:

$$\left(\frac{\rho_{npcm}}{\rho_{host}} \right) (U \cdot \nabla) U = -\nabla P + Pr \nabla^2 u + F_B + F_M \quad (18)$$

Heat equation:

$$Cr(U \cdot \nabla \theta) = \left(\frac{k_{npcm}}{k_{host}} \right) \nabla^2 \theta + Q_M \quad (19)$$

where,

$$F_B = \begin{cases} X: & 0 \\ Y: & Ra \times Pr \left(\frac{\rho_{npcm}}{\rho_{host}} \right) \left(\frac{\beta_{npcm}}{\beta_{host}} \right) \theta \end{cases} \text{ and } F_M = \begin{cases} X: & -Ha^2 Pr \left(\frac{\sigma_{npcm}}{\sigma_{host}} \right) (H_y^2 U - H_x H_y V) \\ Y: & +Ha^2 Pr \left(\frac{\sigma_{npcm}}{\sigma_{host}} \right) (H_x H_y U - H_x^2 V) \end{cases} \quad (20)$$

and

$$Q_M = Ha^2 Ec \left(\frac{\sigma_{npcm}}{\sigma_{host}} \right) (U H_y - V H_x)^2 \quad (21)$$

The dimensionless parameters that are featured in the preceding equations, specifically Hartmann (Ha), Rayleigh (Ra), and Prandtl (Pr) numbers:

$$Ha = \mu_0 H_0 L \sqrt{\frac{\sigma_{host}}{\mu_{host}}}, Ra = \frac{\rho_{host} g \beta_{host} (Th - Tc) L^3}{\alpha_{host} \mu_{host}}, Pr = \frac{\mu_{host}}{\rho_{host} \alpha_{host}} \quad (22)$$

where,

$$\left(\frac{\rho_{npcm}}{\rho_{host}} \right) = (1 - \varphi) + \varphi \left(\frac{\rho_{particle}}{\rho_{host}} \right) \text{ and } \left(\frac{\beta_{npcm}}{\beta_{host}} \right) = (1 - \varphi) + \varphi \left(\frac{\beta_{particle}}{\beta_{host}} \right), \quad (23)$$

Moreover, the expansion of particles is assumed to parallel that of the host fluid, leading to approximate ratios of $(\beta_{npcm}/\beta_{host}) \sim 1$ and $(\rho_{npcm}/\rho_{host}) \sim 0.74$ [43]. Given that the electrical conductivity of PU is negligible in comparison to water, its impact can be overlooked, resulting in $\sigma_{npcm}/\sigma_{host} \sim 1$. The heat capacity ratio, or Cr , is calculated considering factors like nanoparticle concentration, the Stefan number (Ste), and the ratio of sensible heat capacities (κ) as:

$$Cr = \frac{(\rho C_p)_{npcm}}{(\rho C_p)_{host}} = (1 - \varphi) + \frac{\varphi}{Ste \times \delta} \zeta + \varphi \kappa \quad (24)$$

where,

$$Ste = \frac{(\rho C_p)_{host} (Th - Tc) (\rho_{shell} + \iota \rho_{core})}{\alpha_{host} (h_{sf} \rho_{core} \rho_{shell})}, \delta = \frac{\delta T}{(Th - Tc)}, \quad (25)$$

$$Ec = \frac{(\alpha_{host} \mu_{host})}{(\rho C_p)_{host} (Th - Tc) L^2}, \kappa = \frac{(C_p)_{core} + \iota (C_p)_{shell}}{(\rho C_p)_{host} (\rho_{shell} + \iota \rho_{core})},$$

In addition, the non-dimensional fusion function, denoted by ζ , was determined as:

$$\zeta = \frac{\pi}{2} \times \sin \left(\frac{\pi}{\delta} (\theta - \theta_m + \delta/2) \right) \times \begin{cases} 0 & \theta < (\theta_m - \delta/2) \\ 1 & (\theta_m - \delta/2) < \theta < (\theta_m + \delta/2) \\ 0 & \theta > (\theta_m + \delta/2) \end{cases} \quad (26)$$



Moreover, the dimensionless local entropy generation (Sl) relationship can be articulated as follows:

$$S_l = S_U + S_\theta = +\chi_0 \left(\frac{\mu_{npcm}}{\mu_{host}} \right) \left(2 \left(\frac{\partial U}{\partial X} \right)^2 + 2 \left(\frac{\partial V}{\partial Y} \right)^2 + \left(\frac{\partial U}{\partial Y} + \frac{\partial V}{\partial X} \right)^2 \right) + \left(\frac{k_{npcm}}{k_{host}} \right) \left(\left(\frac{\partial \theta}{\partial X} \right)^2 + \left(\frac{\partial \theta}{\partial Y} \right)^2 \right) \quad (27)$$

Here, χ_0 represents the irreversibility parameter in the above relationship, which is defined as:

$$\chi_0 = \frac{\mu_{host} T_0}{k_{host}} \left(\frac{\alpha_{host}}{L(Th - Tc)} \right)^2 \quad (28)$$

The implementation of dimensionless boundary conditions involved $\theta = 0$ and $\theta = 1$ for the cooled and heated walls and $\partial \theta / \partial N = 0$ for the zero-flux curved wall. $U = 0$ across all walls, with $P = 0$ designated at the reference point.

The local ($Nu_l = h_l/k_{host}$) and mean Nusselt numbers at the base wall are viewed as essential parameters for heat transfer, and they can be expressed in the following way:

$$Nu_l = - \left(\frac{k_{npcm}}{k_{host}} \right) \left(\frac{\partial \theta}{\partial N} \right) \bigg|_{Y=0} = -(Nc\varphi + 1) \left(\frac{\partial \theta}{\partial N} \right) \bigg|_{Y=0} \quad (29)$$

and

$$Nu = \int_{L_x}^L Nu_l dL \quad (30)$$

in which the free convection coefficient of heat transfer at the heated wall (h) is utilized. The integration bonds were chosen over the heated wall. Moreover, the Nusselt number was not divided by the non-dimensional length of the hot wall so this parameter denotes the actual dimensionless heat transfer including the surface length effects. The dimensionless average entropy generation (S) is computed by average integration over the solution domain as:

$$S = \frac{\oint S_l dA}{A} \quad (31)$$

Finally, the dimensionless stream function (ω) was introduced as:

$$\nabla^2 \omega = \left(\frac{\partial U}{\partial Y} - \frac{\partial V}{\partial X} \right) \quad (32)$$

where $V = -\partial \omega / \partial X$ and $U = \partial \omega / \partial Y$. The cavity walls were considered as a streamline, $\omega = 0$ [41, 42].

3. Numeric Technique and Model Validation

3.1. Finite element method

The Finite Element Method (FEM) was harnessed to handle the crux equations, the starting states, and the edge values. A weak variant of the core equations, was used to pave the way for the implementation of Gauss quadrature integration at the level of individual elements. This yielded an algebraic system filled with residual equations. To solve these equations, the iterative Newton method was employed, incorporating a damping factor of 0.9 to boost convergence rates [44, 45]. Further, the PARDISO parallel solver was invoked to streamline parallel computations spanning several processing units [46, 47]. The relative error for computational precision was set at less than 1×10^{-4} .

Mesh study

An investigation was carried out to determine the impact of mesh resolution on computational precision, focusing on the study of free convection heat transfer in a NEPCM suspension within a predefined test scenario. The non-dimensional parameters employed in this particular test scenario comprised $Ra = 10^5$, $\theta_f = 0.30$, $Pr = 6.2$, $Ste = 0.30$, $\kappa = 0.33$, $Ec = 10^{-12}$, $\chi_0 = 10^{-4}$, $Nv = 6.0$, $Nc = 6.0$, $Ha = 20$, $Lx = Ly = 0.10$, and $\phi = 0.04$.

To discretize the solution domain, a free-quad form mesh was utilized, with the mesh resolution parameter known as the size number (m) determining the dimensions of the mesh elements. A small value of m corresponds to a more granular, fine mesh, while an increment in m leads to a coarser mesh. The traits of the resulting mesh, which include the quantity of elements, alongside the calculated average Nusselt number and entropy generation, are detailed in Table 3.

The data exhibited in Table 3 presents a persuasive evaluation of the influence of mesh resolution (regulated by the size number m) on entropy generation (S) and the Nusselt number (Nu) in the investigation of the analyzed meshes. As the size number m is incremented, there is an effective reduction in the size of the mesh elements, mirrored by a rise in the quantity of free-quads. From $m = 2$ to $m = 7$, the number of free-quads rises significantly from 2,501 to 30,879. This is indicative of a more refined mesh, giving us a higher resolution computational domain for our study.

Entropy generation (S) displays a rather interesting pattern. As we refine our mesh (increase m), the entropy generation exhibits a slight fluctuation, but eventually stabilizes around the value of 15.768 as we move from $m = 4$ to $m = 7$. This suggests that the system under investigation is on the brink of achieving a mesh-independent solution for entropy generation, hinting that additional refinement of the mesh might not substantially influence the entropy generation outcome. In a similar vein, the Nusselt number (Nu) appears to follow a stabilization trend. With an increase in m , Nu escalates from 5.11 to 5.22. The steady climb and slight variation in Nu propose a gradual convergence towards a definitive value, indicating that a mesh-independent solution is nearing attainment. The error percentage for both S and Nu also showcases a declining trend, further substantiating the idea that a more refined mesh (elevated m value) produces a more accurate computational outcome. As seen, when $m = 5$, the maximum error is less than 0.5% which is quite low and adequate for most of graphical plots. Thus, $m = 5$ was adopted for the simulations.

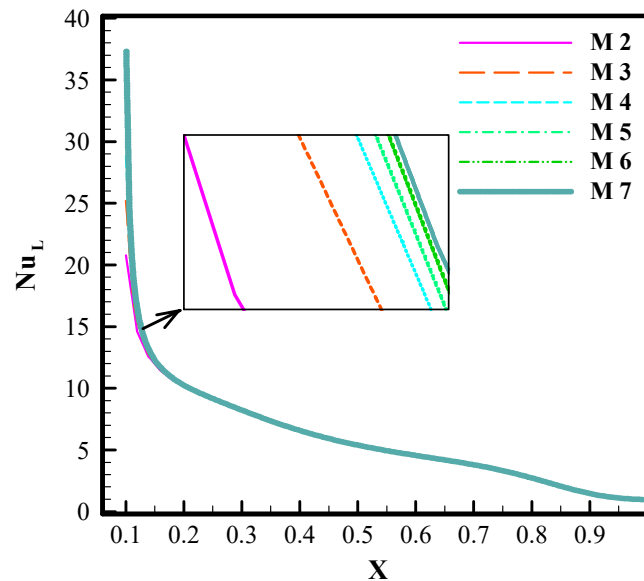
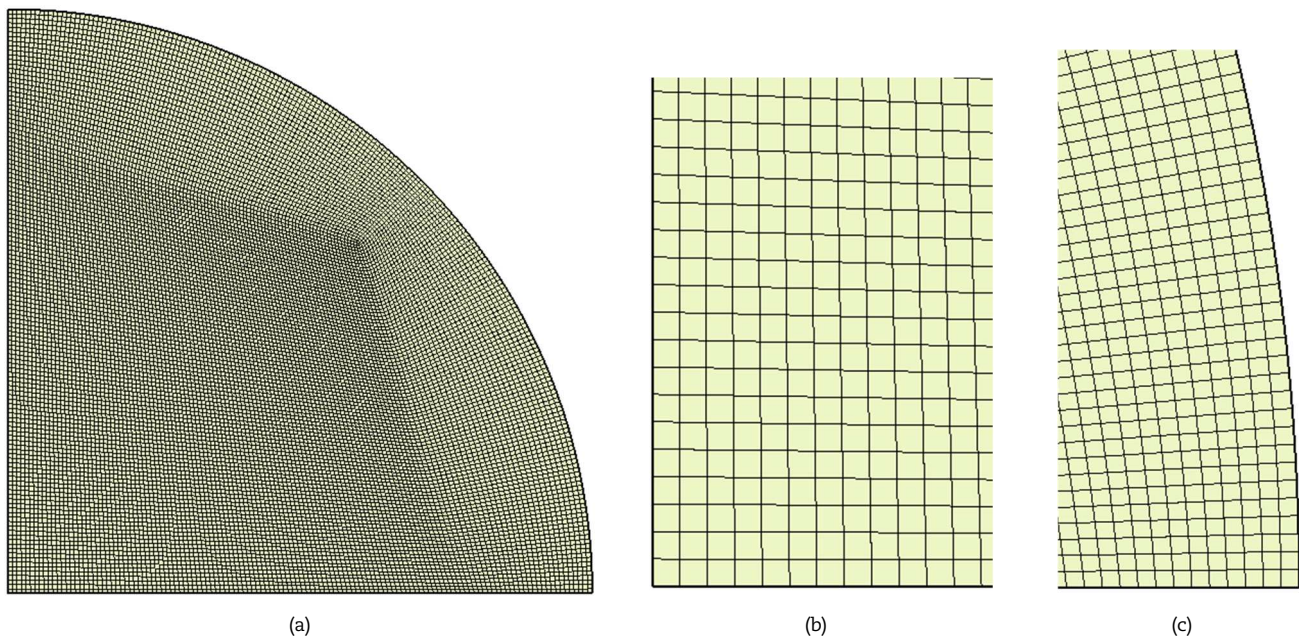


Table 3. An overview of the characteristics of mesh elements, along with the associated values for Nu and S for the scrutinized meshes.

m	Free-quads	S	*Error %	Nu	**Error %
2	2501	15.750	0.123	5.11	2.15
3	5795	15.773	0.023	5.16	1.30
4	10287	15.768	0.009	5.18	0.81
5	15857	15.767	0.015	5.2	0.49
6	22869	15.768	0.009	5.21	0.21
7	30879	15.769	-	5.22	-

*Error % = $100 \times |S - S_{@m=7}| / S_{@m=7}$; **Error % = $100 \times |Nu - Nu_{@m=7}| / Nu_{@m=7}$.

The behavior of the Nusselt number (Nu) can be influenced by several factors, including mesh resolution. At the start of the heated wall ($X = L_x$), which is close to the cold wall, temperature gradients are high. A higher mesh resolution (indicated by an increase in m) allows these gradients to be captured more accurately, resulting in a higher calculated local Nusselt number. However, the increased resolution also decreases the effective length over which this high Nusselt number is observed. Thus, the increase of mesh resolution confines the local Nusselt number into a smaller region. Even though Nu_i might show significant changes due to the mesh refinement, the average Nusselt number which indicates the heat transfer rate might not see a substantial change. This is because the average Nusselt number is obtained by integrating the local Nusselt number over the entire length of the heated wall, considering both regions of high and low Nusselt numbers. Figure 4 shows a view of the adopted mesh with $m = 5$.

**Fig. 3.** Depiction of Nu_i across multiple mesh sizes.**Fig. 4.** A glimpse of the chosen mesh, with an $m = 5$, which is employed for the subsequent calculations:
(a) overall mesh, (b) zoomed mesh at corner, (c) zoomed mesh at right bottom edge.

3.2. Validation of the model

To affirm the accuracy of the implemented code, the results of this study are cross-checked with findings from previously published research. As a first check, Kuehn and Goldstein's [48] experimental study was simulated and the results are shown in Fig. 5. The authors sought to broaden understanding of flow and heat transfer within a horizontal annulus. The close alignment between our numerical results and their experimental data underscores the reliability and precision of the applied code.

Sathiyamoorthy and Chamkha's [49] study on magnetohydrodynamic flow and heat transfer in various heating conditions was considered, particularly their work on natural convection under a uniform magnetic field. For comparative purposes, this study adopted their formulation parameters: $Ha = 50$, $Ra = 10^5$, $Pr = 0.054$, a magnetic angle of 90° , and negligible Ec and ϕ . Figure 6 shows the temperature field, with dots representing Sathiyamoorthy and Chamkha's [49] results and lines indicating results from the current research.

In Ghalambaz et al. [50], the free convection heat transfer in NEPCM suspensions within a square cavity was addressed which serves as a reference point. Their methodology involved a hot left wall, a cold right wall, and insulation on the remaining walls, with isotherms, Cr contours, and streamlines illustrating field variables. Figure 7 juxtaposes the results of the present investigation with the findings of Ghalambaz et al. [33] when $Ra = 10^5$, $\theta_f = 0.3$, $Pr = 6.2$, $Ste = 0.3$, $\kappa = 0.33$, $Nv = 12.5$, $Nc = 23.8$, $\phi = 0.05$, and a negligible Hartmann and Eckert number. As seen, a marked alignment can be seen that underscores the credibility of the present findings.

4. Results and Discussions

Within this segment, the convection heat transfer and heat transfer rate are explored in relation to various influencing factors. These factors include the concentration of NEPCM particles (ranging from 0 to 0.05), the Rayleigh number (ranging from 10^3 to 10^5), the Hartmann number (ranging from 0 to 100), and the fusion temperature for NEPCM particles (ranging from 0.1 to 0.9). The non-dimensional parameters utilized in this investigation remain consistent with those previously documented during the mesh examination. In the event of any modifications or adjustments to these non-dimensional parameters, explicit documentation and reporting will be provided.

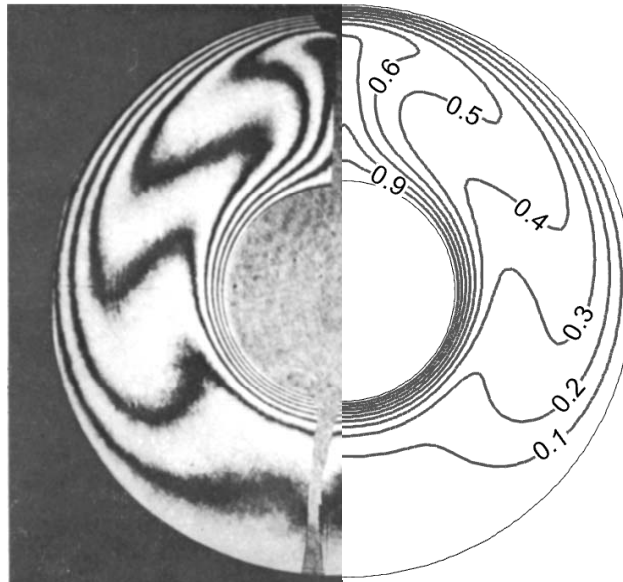


Fig. 5. Comparison between experimental temperature distribution (left) [48] and the current simulations when $\phi = Ha = Ec = 0$, $Pr = 0.706$, $Ra = 4.7 \times 10^4$.

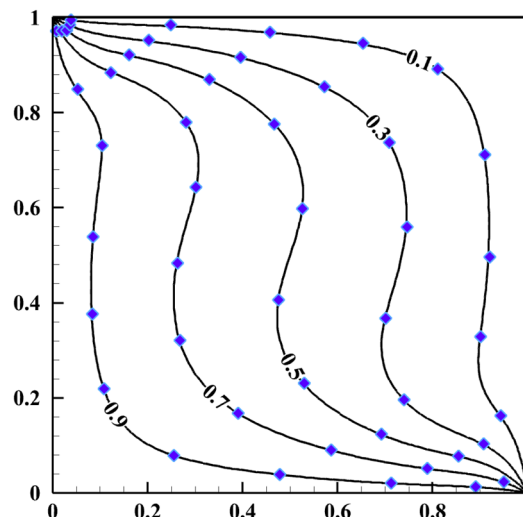


Fig. 6. A cross check between the findings of Sathiyamoorthy and Chamkha [49] and present simulations.



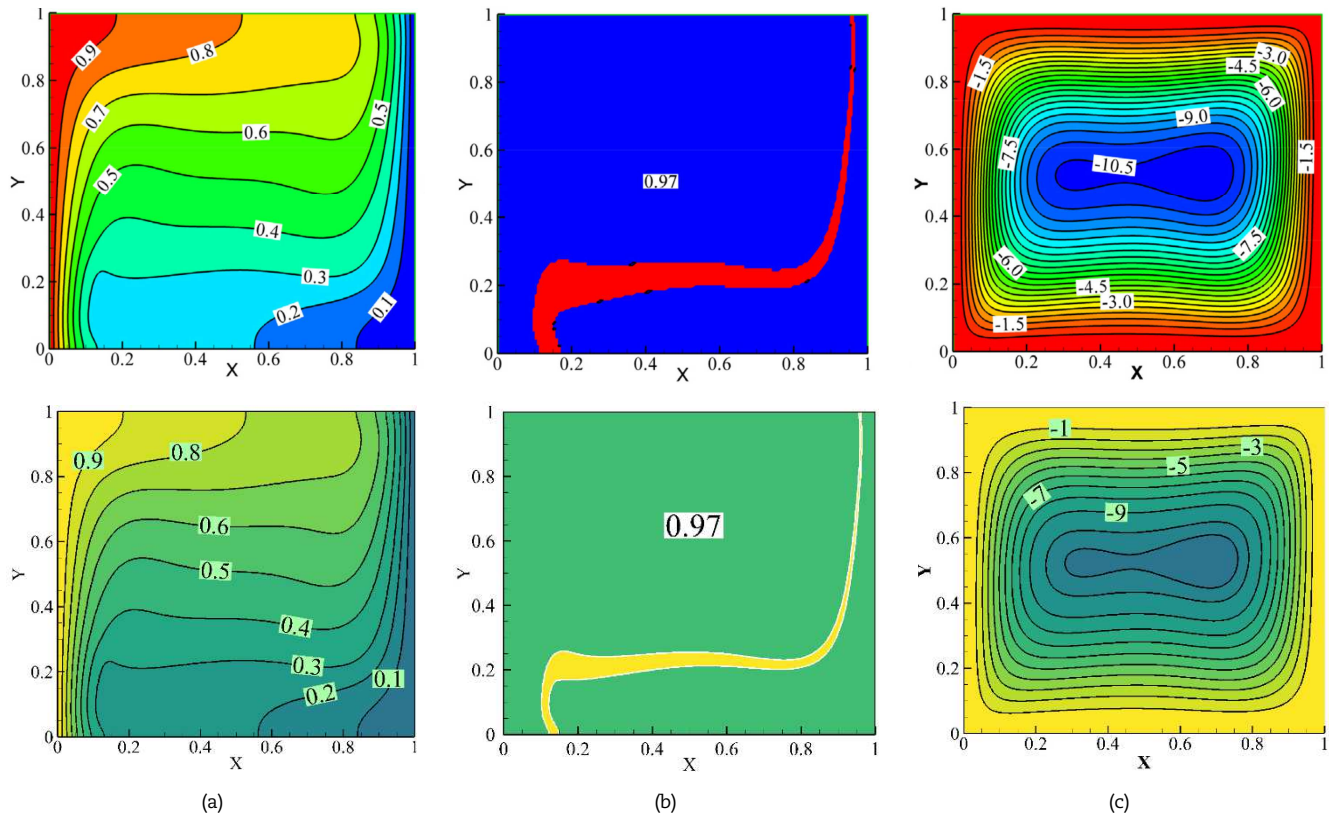


Fig. 7. Contrast between the current study's (a) isotherms (second row), (b) CR contours, and (c) streamlines and those from study Kuehn and Goldstein [48] (first row) regarding NEPCM suspensions' heat transfer within a square cavity.

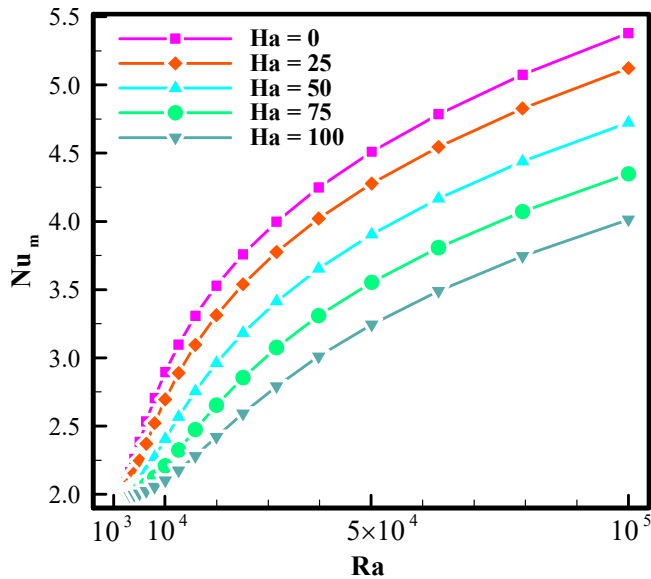


Fig. 8. Average Nu (Nu_m) for different Ra values versus different Ha.

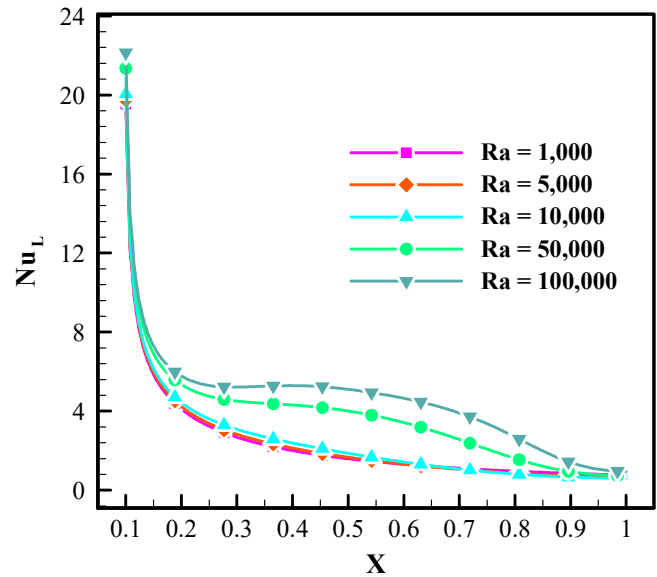


Fig. 9. Local Nusselt number for a range of Ra values at $Ha = 100$.

4.1. Hartmann and Rayleigh number (Ha-Ra)

Figure 8 presents the average Nusselt number (Nu_m) in relation to the Rayleigh number (Ra) for different Hartmann numbers (Ha). An increase in Ra markedly enhances the heat transfer rate, as indicated by Nu_m , whereas a rise in Ha diminishes it. The presence of the magnetic field adds a force against the fluid flow and thus diminishes the natural convection circulation. In such cases, the presence of NEPCM particles could be beneficial through improved thermal conductivity and local augmentation of heat capacity. The local Nusselt number (Nu_L) over the horizontal heated wall is also depicted in Fig 9. Near the start of the wall, where the hot and cold walls are proximate, the heat transfer rate is high. Moving in the positive x -direction, the heat transfer rate tapers off and nears zero by the wall's end. Close to where the hot wall meets the cold wall, heat transfer predominantly occurs through conduction due to the close proximity of the plates and the minimal velocities. As such, Ra variations exert minimal influence on Nu_L . However, at the plate's midpoint, the effect of Ha on heat transfer becomes more pronounced, with increasing Ra causing Nu_L to rise.



For a deeper understanding of how Ra impacts the field variables, Fig. 10 showcases contour maps highlighting isotherms, streamlines, phase transition regions (CR), and entropy generation across varying Rayleigh numbers. For $Ra = 10^3$, flow circulation is relatively weak, with isotherms displaying a quasi-linear progression from the horizontal heated wall to the cold vertical counterpart. Phase transitions are evident around the $\theta_f = 0.3$. Temperature line, corresponding to $\theta_f = 0.3$. Peak entropy generation is localized near the commencement of the hot and cold plates, in proximity to the origin. This aligns with the maximum local Nusselt number as seen in Fig 9. As Ra escalates, flow circulation becomes more vigorous, leading to observable shifts in both isotherms and the phase transition region (evident at $Ra = 5 \times 10^3$). The entropy generation remains largely concentrated near the origin, where substantial temperature gradients coexist with slow fluid velocities—rendering viscous entropy generation almost non-existent. With even greater increases in Ra , this pattern becomes more accentuated. For $Ra = 10^4$, isotherm and CR deviations are clearly visible. Streamlines also exhibit discernible deflections near the corner. Their concave formation adjacent to the origin for $Ra = 10^4$ is a result of the strong Lorenz forces resisting the flow. Notably, a region near the cold surface displays some entropy generation. As Ra reaches 10^5 , this region expands across both the cold and hot plates. Considering a $Ha = 50$, an increase of Ra from 10^3 to 10^5 can boost Nu_m from about 2 to about 4.5, indicating an improvement of approximately 56% in the heat transfer rate.

4.2. Hartmann number (Ha) and fusion temperature (θ_f)

Figure 11 presents both the average and local Nusselt numbers in relation to the Hartmann number, considering different fusion temperatures of nanoparticle cores. For a more comprehensive understanding, Fig. 12 delves deeper into the depiction of the local Nusselt number across varying Hartmann numbers. As observed in Fig. 11, the Nusselt number (Nu_m) decreases with an escalating Ha . However, the influence of fusion temperature on the Nu_m does not follow a linear trend. Notably, the highest Nu_m is observed when $\theta_f = 0.3$. It was discerned from Fig. 10 that at $\theta_f = 0.3$, the phase transition region is roughly equidistant from both the hot and cold plates, though slightly skewed towards the upper portion of the enclosure. This positioning optimally facilitates natural convection flows, signifying that the phase transition region at $\theta_f = 0.3$ is ideally situated for heat transfer between the plates. For a case of $\theta_f = 0.3$, an increase of Ha from 0 to 100 changes Nu_m from 5.38 to 4.04 indicating 25% reduction in heat transfer.

The local Nusselt number curves, across different Ha values, exhibit intriguing characteristics. An increase in Ha initially diminishes the rate of heat transfer at the commencement of the hot wall, particularly near the corner region where the magnetic field's influence is pronounced. Figure 2 provides insights into the intensity and spatial distribution of this magnetic field. As one moves further from the origin (source of magnetism), the impact of Ha on the local Nusselt number recedes swiftly.

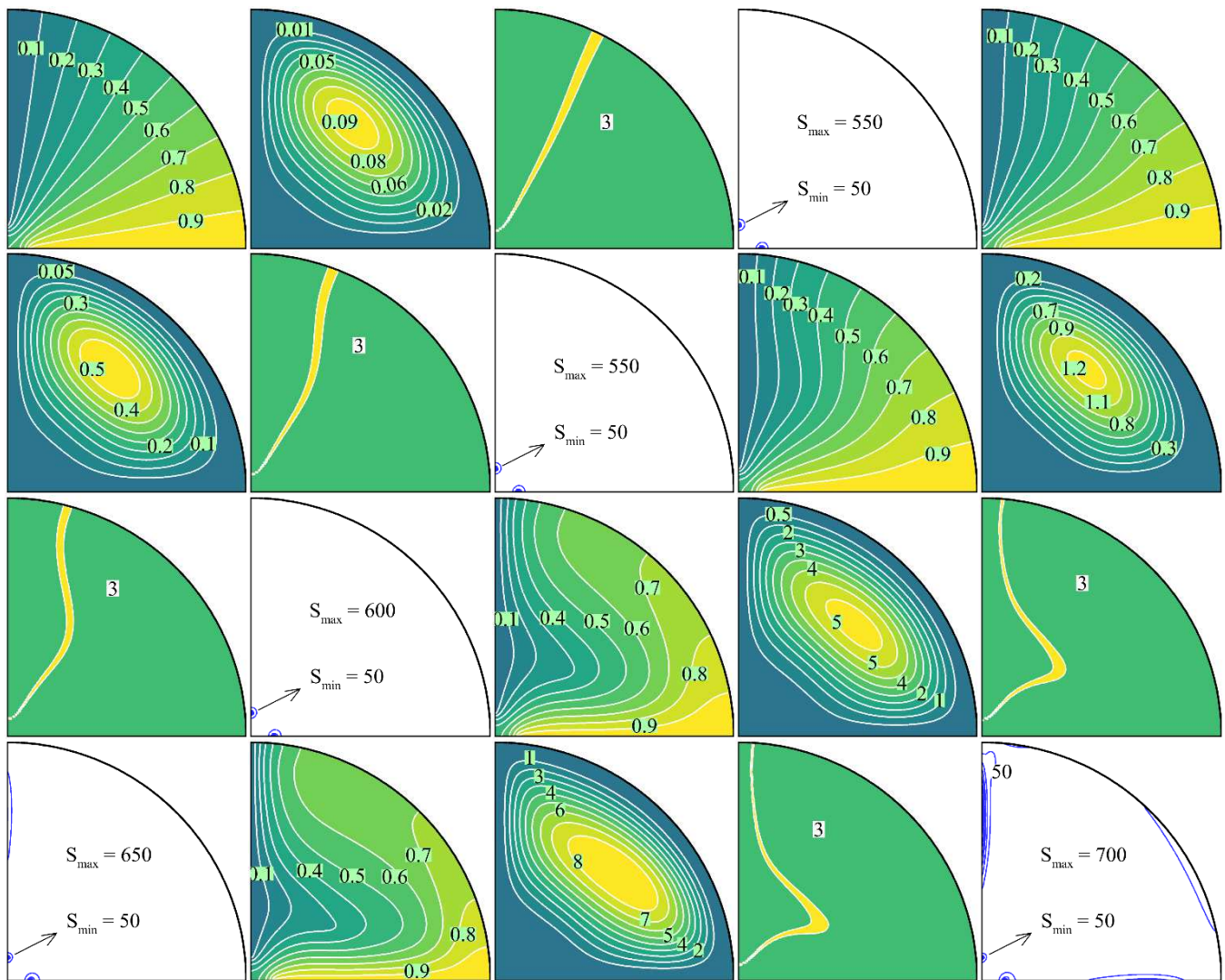


Fig. 10. A comparison of isotherms, streamlines, CR and entropy generation contours at $Ha = 100$ for various Rayleigh numbers: $Ra = 1000, 5000, 10^4, 5 \times 10^4$ and 10^5 .



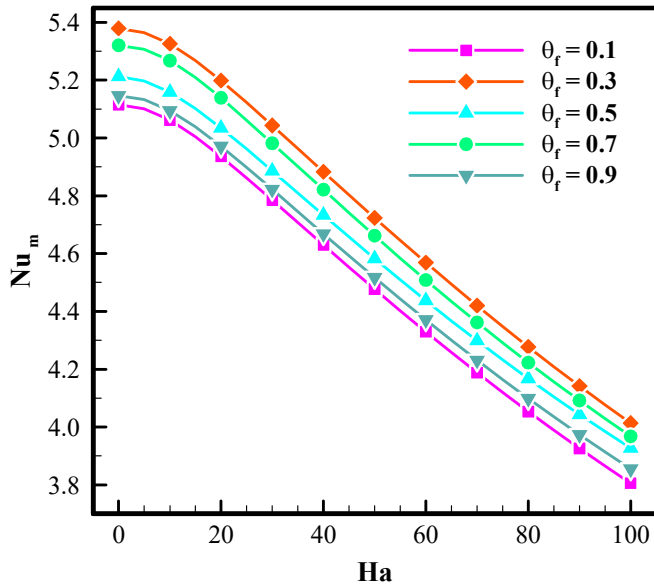


Fig. 11. Average Nusselt number for a range of fusion temperature θ_f and several Hartmann numbers.

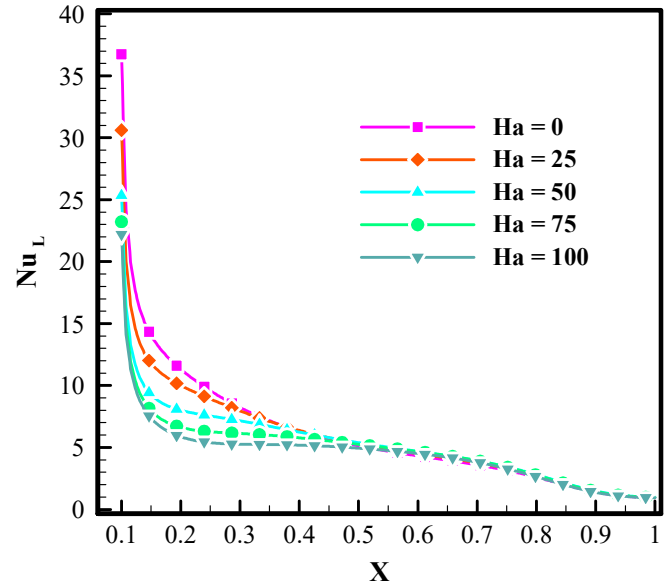


Fig. 12. Local Nusselt number at $\theta_f = 0.25$ for a range of Ha.

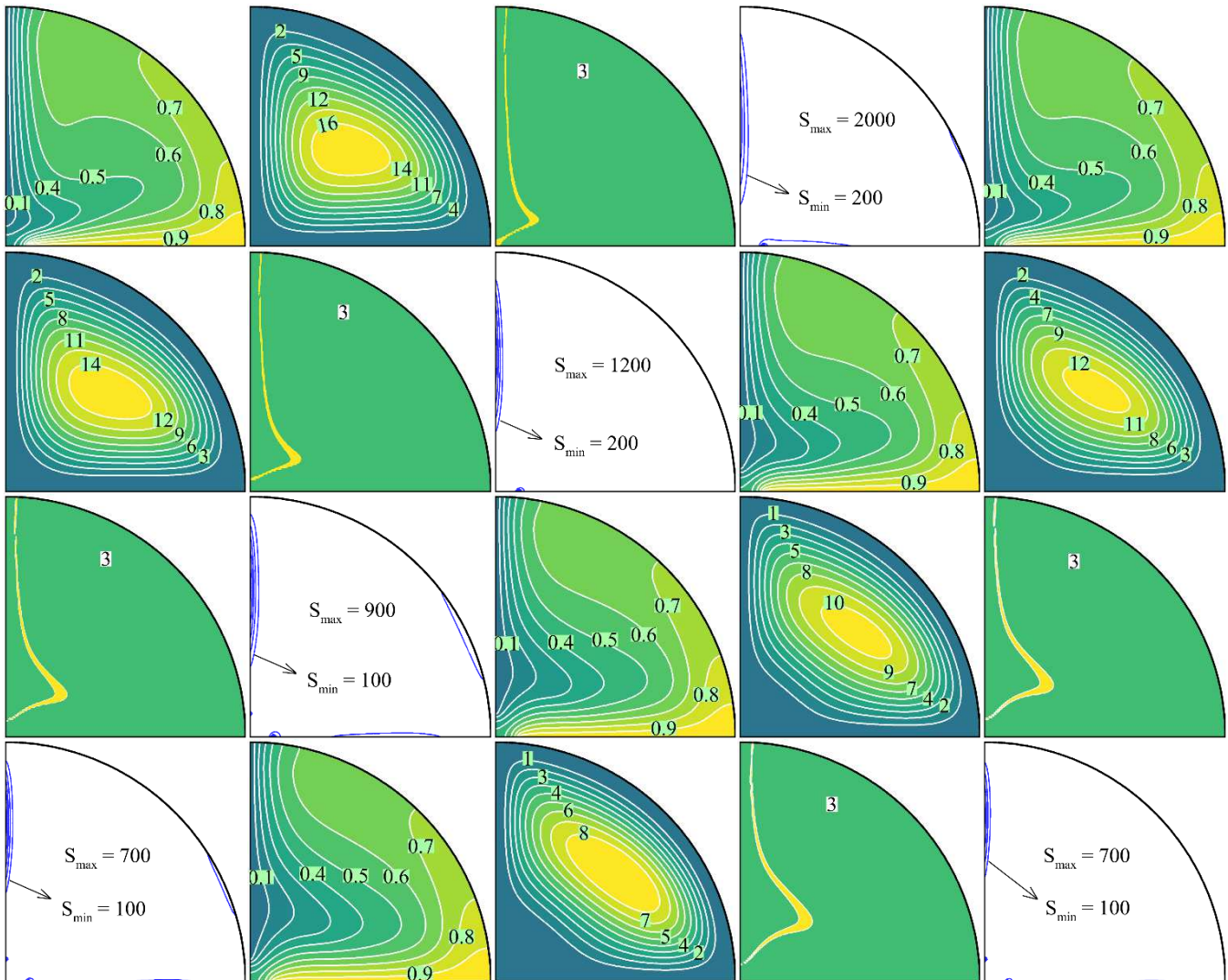


Fig. 13. A comparison of isotherms, streamlines, CR and entropy generation contours at $\theta_f = 0.25$ for several values of Ha, Ha = 0, 25, 50, 75 and 100.



Figure 13 illustrates contour maps for an array of Ha values. Elevating the Ha value introduces subtle modifications to the isotherm patterns, attributable to the direct effect of Ha on streamlines and convection flow. Subsequently, this direct impact induces indirect alterations in the isotherms, mediated by the fluid dynamics. For the same reasons, the phase transition region also undergoes minor shifts with increased Ha . As Ha escalates, streamlines near the corner are deflected away, a phenomenon attributed to the counteractive force exerted by the Lorentz force on the fluid's motion. Furthermore, a rise in Ha lessens entropy generation at the hot wall, as it weakens convection intensity and temperature gradients. With a Hartmann number set at a moderate level of $Ha = 50$, adjusting the fusion temperature from 0.1 to 0.3 results in an increase of the Nusselt number (Nu_m) from 4.5 to 4.75, corresponding to an approximate 5.2% enhancement in the rate of heat transfer.

4.3. NEPCM concentration (ϕ) and fusion temperature (θ_f)

Figure 14 depicts the average Nusselt number as a function of the fusion temperature of nanoparticles and their volume concentration. Meanwhile, Figure 15 delves into the local Nusselt number across various concentrations. Intriguingly, Fig. 14 reveals two optimal values for the fusion temperature: $\theta_f = 0.35$ and $\theta_f = 0.675$ with the global optimum observed at $\theta_f = 0.35$. This observation aligns with the findings from Fig. 11 for $\theta_f = 0.3$. Additionally, a local minimum is discernible around $\theta_f = 0.55$. As the fusion temperature of nanoparticles varies, the corresponding phase transition location does too. The position of phase transition is around the corresponding isotherm lines. The shape and position of the phase change region is depicted in Fig. 16 for some selected phase transition temperatures. With $\theta_f = 0.35$, raising the nanoparticle concentration from 0 to 5% elevates the Nusselt number from 4.4 to 5.4, indicating an approximately 18.5% improvement in heat transfer. Considering an optimum fusion temperature of $\theta_f = 0.3$, riding concentration from 0.03 to 0.05, increases Nu_m by 7.4%. Figure 16 illustrates these phase transition locations. As the fusion temperature elevates, the phase transition region (CR) migrates from the vertical cold wall towards the horizontal hot wall. When dominated by convective heat transfer (evidenced at $Ra = 10^5$), a phase transition region proximate to either the hot or cold wall significantly enhances heat transfer. However, it is noteworthy that fusion temperature exerts a minimal influence on entropy generation.

Increasing the concentration of nanoparticles amplifies the local Nusselt number along the heated wall. This augmentation is most evident near the start of the wall and tapers off towards the right (as x value grows). Such behavior is ascribed to the dynamic viscosity's uptick with a rise in nanoparticle concentrations. Near the beginning of the hot surface, fluid velocity is at its peak, resulting in substantial shear rates. Consequently, there's a robust interaction between the fluid and the hot wall, culminating in an improved local Nusselt number. Conversely, towards the wall's extremity, the majority of the fluid flow ascends, leading to diminished shear rates and fluid velocity. This results in the mitigated influence of nanoparticle concentrations on the local Nusselt number. Considering a fixed concentration of $\phi = 0.05$, change of θ_f from 0.1 to 0.35 can change Nu_m from 5.05 to 5.4 indicating 6.4% improvement in heat transfer.

5. Further Analysis using Neural Networks

The neural networks have shown important applications in recent heat transfer designs [50-52]. Here, to understand the influence of control parameters on the rate of heat transfer better, we utilized a neural network. This network featured three interconnected hidden layers, each with 50 neurons that employed sigmoid activation functions (see Fig. 17). We trained the neural network using a dataset encompassing 600 scenarios, which spanned a set of parameters detailed in the results section. The neural network input encompassed the concentration of NEPCM particles ($0 < \phi < 0.05$), aspect ratio ($1000 < Ra < 100000$), Hartmann number ($0 < Ha < 100$), and fusion temperature θ_f in the range of 0.1 to 0.9. The output of this neural network was the modified Nusselt number (Nu_m). The parameters are consistent with those used in the mesh study unless otherwise specified.

Before the training began, the dataset records underwent random shuffling. Of the entire dataset, we designated 70% for training, 15% for testing, and the remaining 15% for validation. We selected Mean Squared Error (MSE) as the target function and incorporated the Adam optimizer [53] in the process. The training regimen spanned 1000 episodes, each having a batch size of 4. We employed the Standard Scaler method [54] to normalize the dataset. The end results were impressive, recording a loss value of $6.8e-04$ during training and $8.08e-04$ in validation.

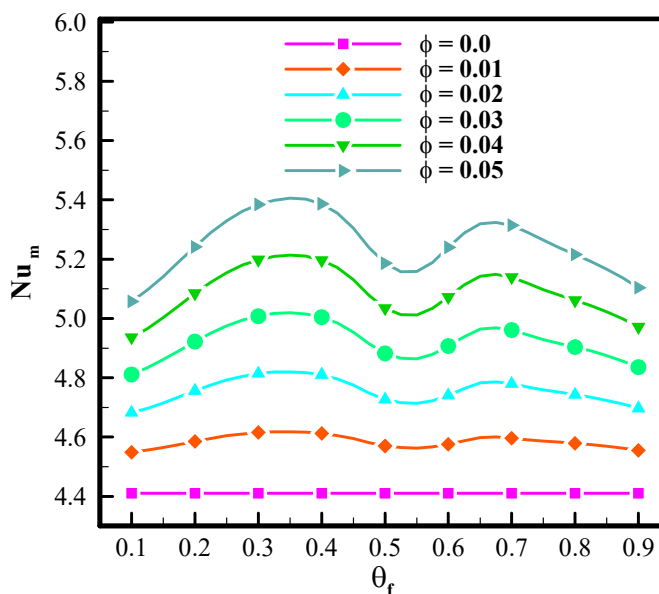


Fig. 14. Average Nusselt number for various θ_f versus ϕ values.

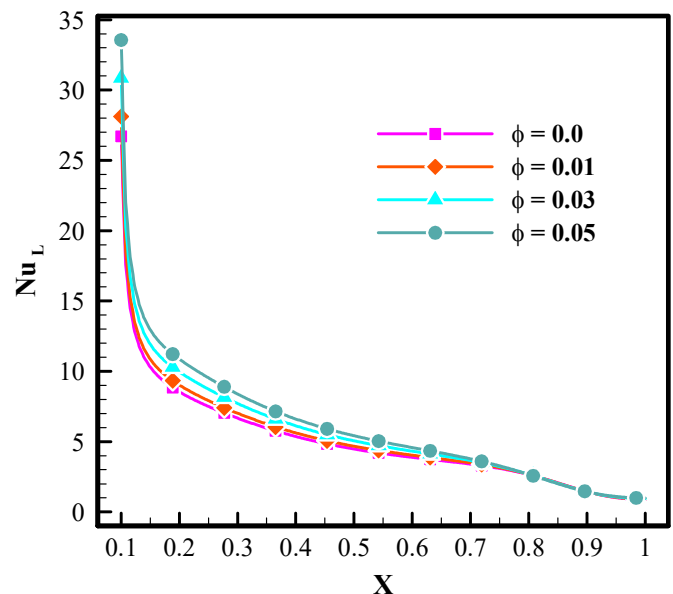


Fig. 15. Local Nusselt number for different ϕ at $\theta_f = 0.25$.



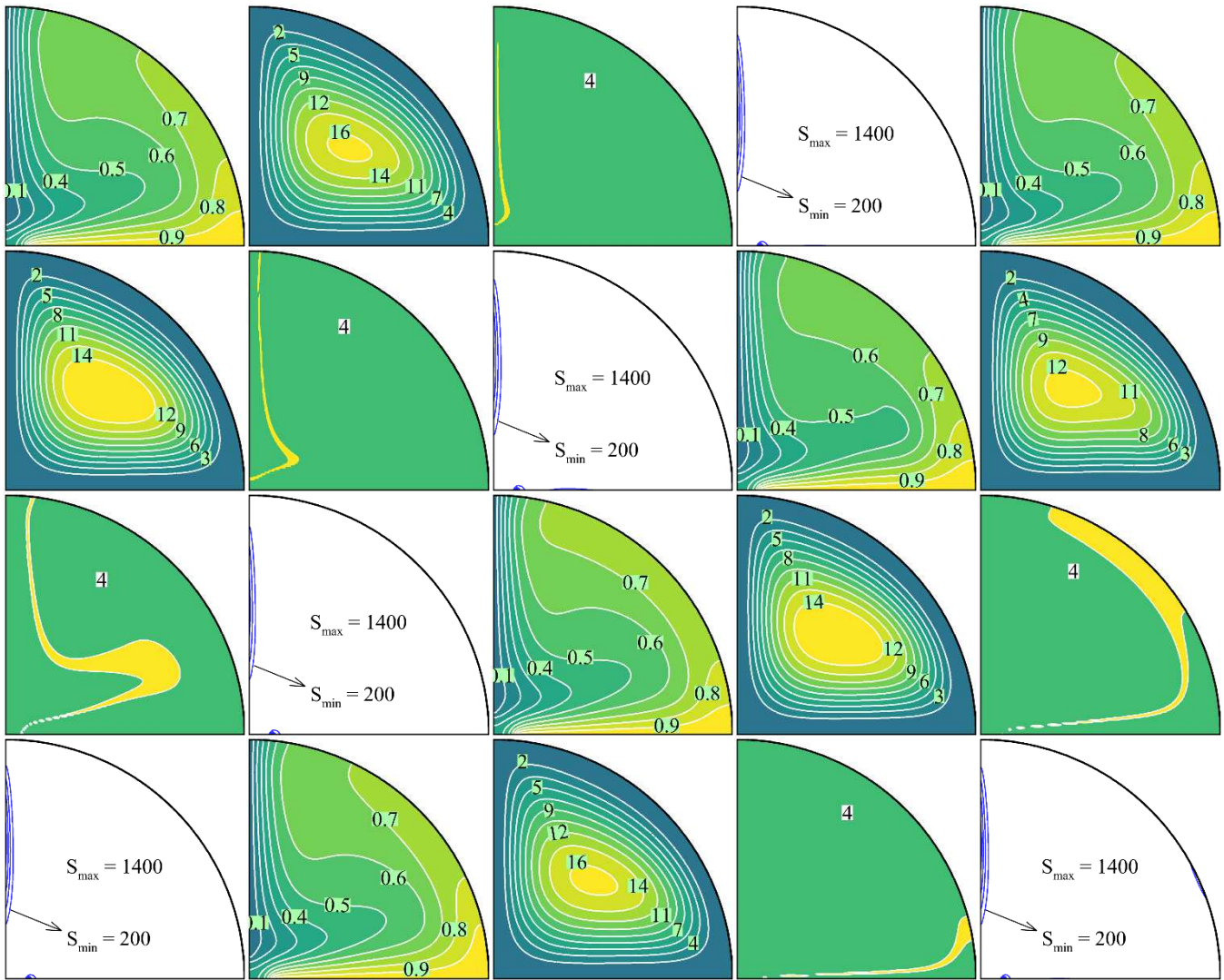


Fig. 16. A comparison of isotherms, streamlines, CR and entropy generation contours at $\phi = 0.05$ for various θ_f where $\theta_f = 0.1$ (first row), 0.25 (second row), 0.75 (third row), and 0.9 (forth row).

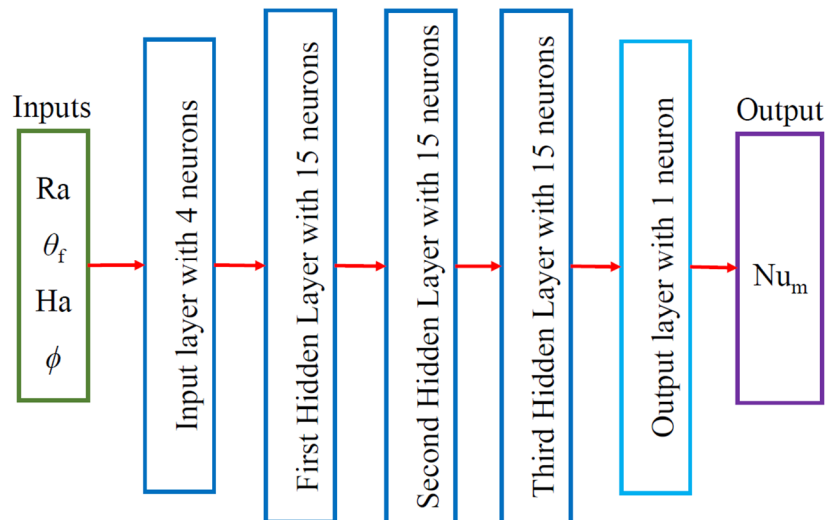


Fig. 17. Diagram illustrating the neural network (NN) architecture in use.

Figure 18 portrays the trajectory of the MSE error during various epochs for the training, testing, and validation datasets, highlighting a continuous decrease as the epochs went by. Figure 19, on the other hand, compares the predicted values against the real test data, underlining the efficacy of the model. Leveraging the capabilities of the neural network, which can now adeptly forecast the influence of input parameters on the rate of heat transfer (Nu_m), we have produced contour diagrams to showcase the effects of control parameters.



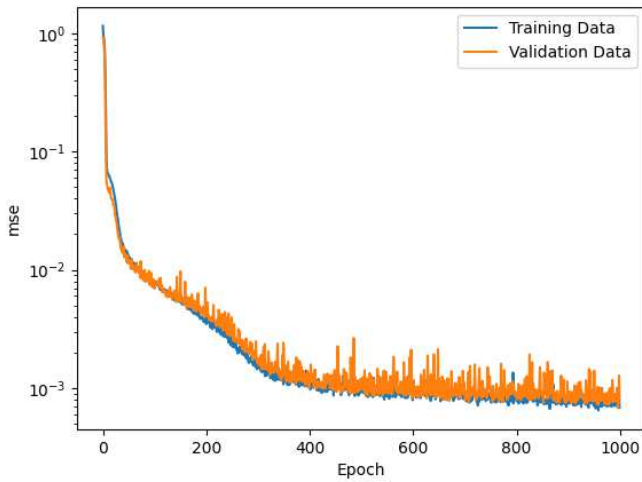


Fig. 18. Epoch-wise representation of training and validation data.

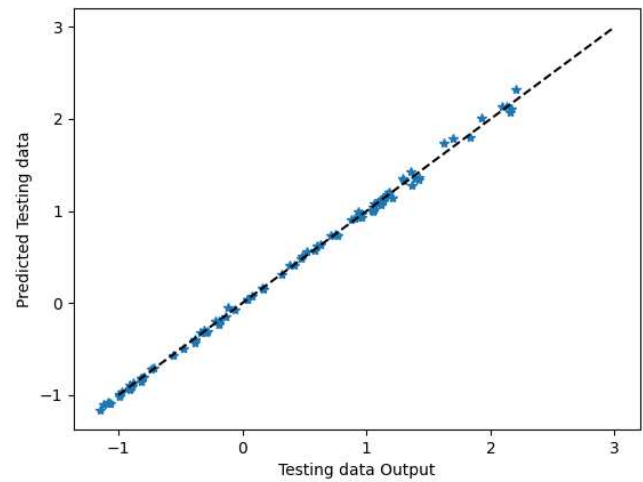


Fig. 19. Comparison of forecasted test data with actual test values.

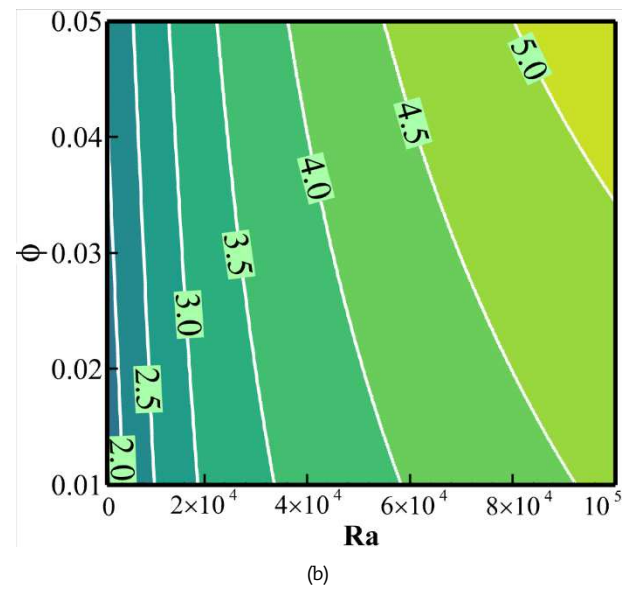
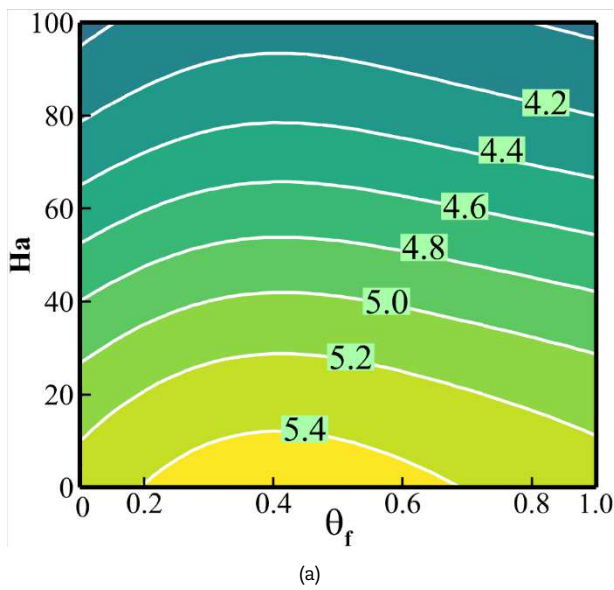


Fig. 20. Predicted Nu_m values across varying control parameters: (a) θ_f -Ha contour at $\phi = 0.05$ and $Ra = 10^5$ and (b) ϕ -Ra contour with $\theta_f = 0.3$ and $Ha = 20$.

Figures 20(a) and 20(b) present contour diagrams of the modified Nusselt number (Nu_m) plotted against the Hartmann number (Ha) and fusion temperature (θ_f), and NEPCM concentration (ϕ) versus Rayleigh number (Ra), respectively. These visual representations elucidate the heat transfer dynamics (Nu_m) under various combinations of controlling parameters. Direct numerical simulations for generating such contours are computationally intensive and can be quite time-consuming. In contrast, the well-trained neural network efficiently generated these visuals within mere seconds. In Fig. 20(a), it is notable that as Ha increases, Nu_m tends to decrease. Furthermore, there appears to be an optimal fusion temperature range around $\theta_f = 0.35$ - 0.4 . An elevation in Ha nudges the optimal fusion temperature from 0.4 closer to 0.35 . Figure 20(b) depicts that increases in both Ra and ϕ lead to a proportional surge in Nu_m . Especially at higher Ra values, even minute variations in ϕ can lead to a marked rise in Nu_m .

6. Conclusions

In this investigation, the heat transfer dynamics of a quadrantal circular enclosure filled with NEPCM suspension is meticulously explored. The study focuses on the interplay of different factors on heat transfer, emphasizing buoyancy-driven natural convection, with the nanoparticles undergoing phase transitions that significantly alter the fluid's thermophysical properties. The nanoparticles have a core of PCM, which shifts through various states - solid, liquid, or undergoing a phase change - dependent on their environment within the host fluid. Additionally, magnetic influences are incorporated into the study. The study emphasizes how the nanoparticles, undergoing phase transitions, alter NEPCM suspension's thermophysical attributes, directly affecting localized heat capacity. Parameters such as the concentration of NEPCM particles, the Rayleigh number, the Hartmann number, and the fusion temperature for NEPCM particles are critical determinants of heat transfer dynamics. The key findings can be listed as follows:

- As the Rayleigh number increases, the heat transfer rate (represented by the Nusselt number) improves. However, an escalation in the Hartmann number diminishes this rate, owing to the Lorenz force's impact on fluid velocity and, consequently, convection.
- At a Hartmann number of $Ha = 50$, increasing the fusion temperature from 0.1 to 0.3 raises the Nusselt number from 4.5 to 4.75 , boosting heat transfer by about 5.2% . Optimal fusion temperature values have been identified at $\theta_f = 0.35$ and $\theta_f = 0.675$,



which are crucial for heat transfer dynamics. The phase transition region shifts depending on the fusion temperature, affecting heat transfer rates. Maintaining a constant 5% concentration of nanoparticles and adjusting the volume fraction (θ_f) from 0.1 to 0.35 results in an increase in the Nusselt number (Nu) from 5.05 to 5.4, demonstrating a 6.4% enhancement in heat transfer.

- The concentration of nanoparticles in the fluid impacts the rate of heat transfer. Specifically, increasing the concentration of nanoparticles enhances the local Nusselt number, especially at the start of the wall. At $\theta_f = 0.35$, boosting nanoparticle concentration from 0 to 5% increases Nu_m from 4.4 to 5.4, marking an 18.5% heat transfer enhancement.
- A neural network model has been developed and trained to predict the influence of input parameters on the rate of heat transfer. This model proves to be highly accurate, as showcased by a comparison between predicted values and real test data.
- The neural network's capabilities highlight the effects of control parameters through contour diagrams, providing insights into heat transfer dynamics under varied controlling parameters. This approach is advantageous as it negates the need for computationally intensive direct numerical simulations.

In essence, the research uncovers intricate relationships between several factors influencing heat transfer in a NEPCM suspension-filled enclosure. The findings shed light on the significant potential of nanoparticles, particularly those undergoing phase transitions, in enhancing cooling efficiencies and energy storage. Moreover, the efficient utilization of neural networks in forecasting heat transfer dynamics offers a promising avenue for future studies and applications.

Author Contributions

The authors confirmed the contribution to this article as follows: M. Ghalambaz: Conceptualization, Methodology, Software, Validation, Formal analysis, Data Curation. I. Pop: Original draft preparation, Investigation, Writing - Review & Editing. M. Sheremet: Original draft preparation, Investigation, Formal analysis, Data Curation, Writing - Review & Editing. M.H. Ali: Methodology, Formal analysis, Original draft preparation, Data curation, Software, Writing - Review & Editing. M. Ghalambaz: Methodology, Writing - Review & Editing, Supervision. The manuscript was written through the contribution of all authors. All authors discussed the results, reviewed, and approved the final version of the manuscript.

Acknowledgments

Not applicable.

Conflict of Interest

The authors declared no potential conflicts of interest concerning the research, authorship, and publication of this article.

Funding

The work of Ioan Pop has been supported from the Grant PN-III-P4-PCE-2021-0993, UEFISCDI, Romania. The research of Mikhail Sheremet and Mohammad Ghalambaz was supported by the Tomsk State University Development Programme (Priority-2030).

Data Availability Statements

The datasets are available from the corresponding author on reasonable request.


References


- [1] Favakeh, A., Khademi, A., Shafii, M. B., Experimental investigation of the melting process of immiscible binary phase change materials, *Heat Transfer Engineering*, 44(2), 2023, 154-174.
- [2] Khademi, A., Abtahi Mehrjardi, S. A., Said, Z., Chamkha, A. J., Heat Transfer Improvement in a Thermal Energy Storage System using Auxiliary Fluid Instead of Nano-PCM in an Inclined Enclosure: A Comparative Study, *Journal of Applied and Computational Mechanics*, 9(2), 2023, 475-486.
- [3] Shank, K., Tiari, S., A review on active heat transfer enhancement techniques within latent heat thermal energy storage systems, *Energies*, 16(10), 2023, 4165.
- [4] Yesilyurt, M. K., Çomaklı, Ö., Encapsulated phase change material slurries as working fluid in novel photovoltaic thermal liquid systems: a comprehensive review, *Iranian Journal of Science and Technology, Transactions of Mechanical Engineering*, 47(4), 2023, 1275-1305.
- [5] Ghalambaz, S., A Scientometric Study of Nano Encapsulated Phase Change Material (NEPCM): Trends and Categories, *Journal of Nanofluids*, 13(4), 2024, 985-998.
- [6] Sharma, H. K., Kumar, S., Kumar, S., Verma, S. K., Performance investigation of flat plate solar collector with nanoparticle enhanced integrated thermal energy storage system, *Journal of Energy Storage*, 55, 2022, 105681.
- [7] Alhashash, A., Saleh, H., Enhancement of conjugate heat transfer in an enclosure by utilizing water and nano encapsulated phase change materials with active cylinder, *Journal of Energy Storage*, 66, 2023, 107422.
- [8] Almutairi, K., Cooling three integrated circuits by embedding them inside an inclined cavity using nano-encapsulated phase change material, *Journal of Energy Storage*, 52, 2022, 104837.
- [9] Ghalambaz, M., Jin, H., Bagheri, A., Younis, O., Wen, D., Convective Flow and Heat Transfer of Nano-Encapsulated Phase Change Material (NEPCM) Dispersions along a Vertical Surface, *Facta Universitatis, Series: Mechanical Engineering*, 20(3), 2022, 519-538.
- [10] Zhang, K., Wang, J., Xu, L., Xie, H., Guo, Z., Preparation and thermal characterization of n-octadecane/pentafluorostyrene nanocapsules for phase-change energy storage, *Journal of Energy Storage*, 35, 2021, 102327.
- [11] Shajahan, M. I., Narayana, D. R., Radha Krishnan, N. S., Michael, J. J., Evaluation of efficiency of double slope solar still and drinking water yield using silver nanoparticle mixed with phase change material, *Energy Sources, Part A: Recovery, Utilization, and Environmental Effects*, 44(4), 2022, 8679-8693.
- [12] Jain, A., Parhizi, M., Theoretical analysis of phase change heat transfer and energy storage in a spherical phase change material with encapsulation, *International Journal of Heat and Mass Transfer*, 185, 2022, 122348.
- [13] Qaderi, A., Veysi, F., Modelling and optimisation of a battery thermal management system with nano encapsulated phase change material slurry for 18650 Li-ion batteries, *Thermal Science and Engineering Progress*, 37, 2023, 101552.
- [14] Cao, Y., Farouk, N., Aayed, H., Aly, A. A., Jarad, F., Dahari, M., Wae-hayee, M., Saleh, B., Heat transfer improvement between a pair of heater and cooler inside an energy storage by using nano-encapsulated phase change material/water: A numerical modeling, *Case Studies in Thermal Engineering*, 30, 2022, 101770.
- [15] Golab, E., Goudarzi, S., Kazemi-Varnamkhasti, H., Amigh, H., Ghaemi, F., Baleanu, D., Karimipour, A., Investigation of the effect of adding nano-encapsulated phase change material to water in natural convection inside a rectangular cavity, *Journal of Energy Storage*, 40, 2021, 102699.




- [16] Aly, A. M., Lewis, R. W., Alsedias, N., Effects of magnetic field and thermal radiation on double diffusion of solid phase in the two connected circular cylinders suspended by NEPCM and porous media, *Journal of Porous Media*, 26(5), 2023, 121-138.
- [17] Abderrahmane, A., Younis, O., Al-Khaleel, M., Laidoudi, H., Akkurt, N., Guedri, K., Marzouki, R., 2D MHD mixed convection in a zigzag trapezoidal thermal energy storage system using NEPCM, *Nanomaterials*, 12(19), 2022, 3270.
- [18] Jiang, Z., Shu, J., Ge, Z., Jiang, Z., Wang, M., Ge, X., Preparation and performance of magnetic phase change microcapsules with organic-inorganic double shell, *Solar Energy Materials and Solar Cells*, 240, 2022, 111716.
- [19] Shin, D. H., Kim, S., Karng, S. W., Shin, Y., Development of a new type of PCM thermal capsule transport system, *International Journal of Heat and Mass Transfer*, 183, 2022, 122034.
- [20] Wang, X., Zhang, C., Wang, K., Huang, Y., Chen, Z., Highly efficient photothermal conversion capric acid phase change microcapsule: Silicon carbide modified melamine urea formaldehyde, *Journal of Colloid and Interface Science*, 582, 2021, 30-40.
- [21] Aly, A. M., Raizah, Z., Ghalambaz, M., The magnetic field on thermosolutal convection in an annulus between two super ellipses, *Waves in Random and Complex Media*, 2022, 1-20.
- [22] Raizah, Z., Aly, A. M., Effect of dual-rotation on MHD natural convection of NEPCM in a hexagonal-shaped cavity based on time-fractional ISPH method, *Scientific Reports*, 11(1), 2021, 22687.
- [23] Alazzam, A., Qasem, N. A., Aissa, A., Abid, M. S., Guedri, K., Younis, O., Natural convection characteristics of nano-encapsulated phase change materials in a rectangular wavy enclosure with heating element and under an external magnetic field, *Journal of Energy Storage*, 57, 2023, 106213.
- [24] Aly, A. M., Alsedais, N., Natural convection of NEPCM in a partial porous H-shaped cavity: ISPH simulation, *International Journal of Numerical Methods for Heat & Fluid Flow*, 33(6), 2023, 2232-2249.
- [25] Shehzad, S., Alshuraiaan, B., Kamel, M. S., Izadi, M., Ambreen, T., Influence of fin orientation on the natural convection of aqueous-based nano-encapsulated PCMs in a heat exchanger equipped with wing-like fins, *Chemical Engineering and Processing-Process Intensification*, 160, 2021, 108287.
- [26] Ahmed, S. E., Khamis, A. K., Exploration of the entropy due to the nano-encapsulated phase change materials (NEPCMs) within oblique prismatic containers, *Physica Scripta*, 96(11), 2021, 115204.
- [27] Aly, A. M., Mohamed, E. M., El-Amin, M. F., Alsedais, N., Double-diffusive convection between two different phases in a porous infinite-shaped enclosure suspended by nano encapsulated phase change materials, *Case Studies in Thermal Engineering*, 26, 2021, 101016.
- [28] Aly, A. M., Hyder, A.-A., Alsedias, N., Time-Conformable fractal systems of natural convection of tall fin inside two circular cylinders suspended by NEPCM, *Alexandria Engineering Journal*, 61(12), 2022, 12311-12328.
- [29] Raizah, Z., Aly, A. M., Dual convection of NEPCM inside an annulus between two circular cylinders mounted on rectangles, *Alexandria Engineering Journal*, 72, 2023, 415-429.
- [30] Athanasopoulos, N., Baltopoulos, A., Matzakou, M., Vavouliotis, A., Kostopoulos, V., Electrical conductivity of polyurethane/MWCNT nanocomposite foams, *Polymer Composites*, 33(8), 2012, 1302-1312.
- [31] Dutta, S., Pati, S., Baranyi, L., Numerical analysis of magnetohydrodynamic natural convection in a nanofluid filled quadrantal enclosure, *Case Studies in Thermal Engineering*, 28, 2021, 101507.
- [32] Barlak, S., Sara, O. N., Karaipekli, A., Yapici, S., Thermal conductivity and viscosity of nanofluids having nanoencapsulated phase change material, *Nanoscale and Microscale Thermophysical Engineering*, 20(2), 2016, 85-96.
- [33] Ghalambaz, M., Chamkha, A. J., Wen, D., Natural convective flow and heat transfer of nano-encapsulated phase change materials (NEPCMs) in a cavity, *International Journal of Heat and Mass Transfer*, 138, 2019, 738-749.
- [34] Ghalambaz, M., Zadeh, S. M. H., Mehryan, S., Pop, I., Wen, D., Analysis of melting behavior of PCMs in a cavity subject to a non-uniform magnetic field using a moving grid technique, *Applied Mathematical Modelling*, 77, 2020, 1936-1953.
- [35] Sheikholeslami, M., Vajravelu, K., Nanofluid flow and heat transfer in a cavity with variable magnetic field, *Applied Mathematics and Computation*, 298, 2017, 272-282.
- [36] Selimefendigil, F., Öztürk, H. F., Chamkha, A. J., MHD mixed convection and entropy generation of nanofluid filled lid driven cavity under the influence of inclined magnetic fields imposed to its upper and lower diagonal triangular domains, *Journal of Magnetism and Magnetic Materials*, 406, 2016, 266-281.
- [37] Chen, B., Wang, X., Zeng, R., Zhang, Y., Wang, X., Niu, J., Li, Y., Di, H., An experimental study of convective heat transfer with microencapsulated phase change material suspension: laminar flow in a circular tube under constant heat flux, *Experimental Thermal and Fluid Science*, 32(8), 2008, 1638-1646.
- [38] Khanafer, K., Vafai, K., A critical synthesis of thermophysical characteristics of nanofluids, *International Journal of Heat and Mass Transfer*, 54(19-20), 2011, 4410-4428.
- [39] Chai, L., Shaukat, R., Wang, L., Wang, H. S., A review on heat transfer and hydrodynamic characteristics of nano/microencapsulated phase change slurry (N/MPCS) in mini/microchannel heat sinks, *Applied Thermal Engineering*, 135, 2018, 334-349.
- [40] Seyf, H. R., Zhou, Z., Ma, H., Zhang, Y., Three dimensional numerical study of heat-transfer enhancement by nano-encapsulated phase change material slurry in microtube heat sinks with tangential impingement, *International Journal of Heat and Mass Transfer*, 56(1-2), 2013, 561-573.
- [41] Zaraki, A., Ghalambaz, M., Chamkha, A. J., Ghalambaz, M., De Rossi, D., Theoretical analysis of natural convection boundary layer heat and mass transfer of nanofluids: effects of size, shape and type of nanoparticles, type of base fluid and working temperature, *Advanced Powder Technology*, 26(3), 2015, 935-946.
- [42] Chamkha, A., Doostanidezfuli, A., Izadpanahi, E., Ghalambaz, M., Phase-change heat transfer of single/hybrid nanoparticles-enhanced phase-change materials over a heated horizontal cylinder confined in a square cavity, *Advanced Powder Technology*, 28(2), 2017, 385-397.
- [43] Mehryan, S., Ghalambaz, M., Gargari, L. S., Hajjar, A., Sheremet, M., Natural convection flow of a suspension containing nano-encapsulated phase change particles in an eccentric annulus, *Journal of Energy Storage*, 28, 2020, 101236.
- [44] Kelley, C. T., *Solving nonlinear equations with Newton's method*, SIAM, 2003.
- [45] Deufilhard, P., *Newton methods for nonlinear problems: affine invariance and adaptive algorithms*, Springer Science & Business Media, 2005.
- [46] Bollhöfer, M., Schenk, O., Janalik, R., Hamm, S., Gullapalli, K., State-of-the-art sparse direct solvers, *Parallel Algorithms in Computational Science and Engineering*, 2020, 3-33.
- [47] Bollhöfer, M., Eftekhari, A., Scheidegger, S., Schenk, O., Large-scale sparse inverse covariance matrix estimation, *SIAM Journal on Scientific Computing*, 41(1), 2019, A380-A401.
- [48] Kuehn, T., Goldstein, R., An experimental and theoretical study of natural convection in the annulus between horizontal concentric cylinders, *Journal of Fluid Mechanics*, 74(4), 1976, 695-719.
- [49] Sathiyamoorthy, M., Chamkha, A. J., Natural convection flow under magnetic field in a square cavity for uniformly (or) linearly heated adjacent walls, *International Journal of Numerical Methods for Heat & Fluid Flow*, 22(5), 2012, 677-698.
- [50] Mehrjardi, S. A. A., Khademi, A., Fazli, M., Optimization of a thermal energy storage system enhanced with fins using generative adversarial networks method, *Thermal Science and Engineering Progress*, 49, 2024, 102471.
- [51] Edalatifar, M., Tavakoli, M. B., Ghalambaz, M., Setoudeh, F., Using deep learning to learn physics of conduction heat transfer, *Journal of Thermal Analysis and Calorimetry*, 146, 2021, 1435-1452.
- [52] Loyola-Fuentes, J., Nazemzadeh, N., Diaz-Bejarano, E., Mancin, S., Coletti, F., A framework for data regression of heat transfer data using machine learning, *Applied Thermal Engineering*, 248, 2024, 123043.
- [53] Jais, I. K. M., Ismail, A. R., Nisa, S. Q., Adam optimization algorithm for wide and deep neural network, *Knowledge Engineering and Data Science*, 2(1), 2019, 41-46.
- [54] StandardScaler. Scikit. (n.d.), <https://scikit-learn.org/stable/modules/generated/sklearn.preprocessing.StandardScaler.html>, 2024.


ORCID iD

Mehdi Ghalambaz  <https://orcid.org/0000-0001-8762-5510>

Ioan Pop  <https://orcid.org/0000-0002-0660-6543>

Mikhail Sheremet  <https://orcid.org/0000-0002-4750-0227>



Mohammed Hasan Ali  <https://orcid.org/0000-0001-7963-0918>

Mohammad Ghalambaz  <https://orcid.org/0000-0003-0965-2358>



© 2024 Shahid Chamran University of Ahvaz, Ahvaz, Iran. This article is an open access article distributed under the terms and conditions of the Creative Commons Attribution-NonCommercial 4.0 International (CC BY-NC 4.0 license) (<http://creativecommons.org/licenses/by-nc/4.0/>).

How to cite this article: Ghalambaz M., et al. Numerical and Artificial Neural Network Analysis of Magnetohydrodynamic Natural Convection in a Nano-encapsulated Phase Change Suspension Filled Quadrantal Circular Enclosure, *J. Appl. Comput. Mech.*, xx(x), 2024, 1–17. <https://doi.org/10.22055/jacm.2024.47986.4891>

Publisher's Note Shahid Chamran University of Ahvaz remains neutral with regard to jurisdictional claims in published maps and institutional affiliations.

